Volume 18
Number 3
22 January 2026
Pages 1107-1678

Nanoscale

rsc.li/nanoscale

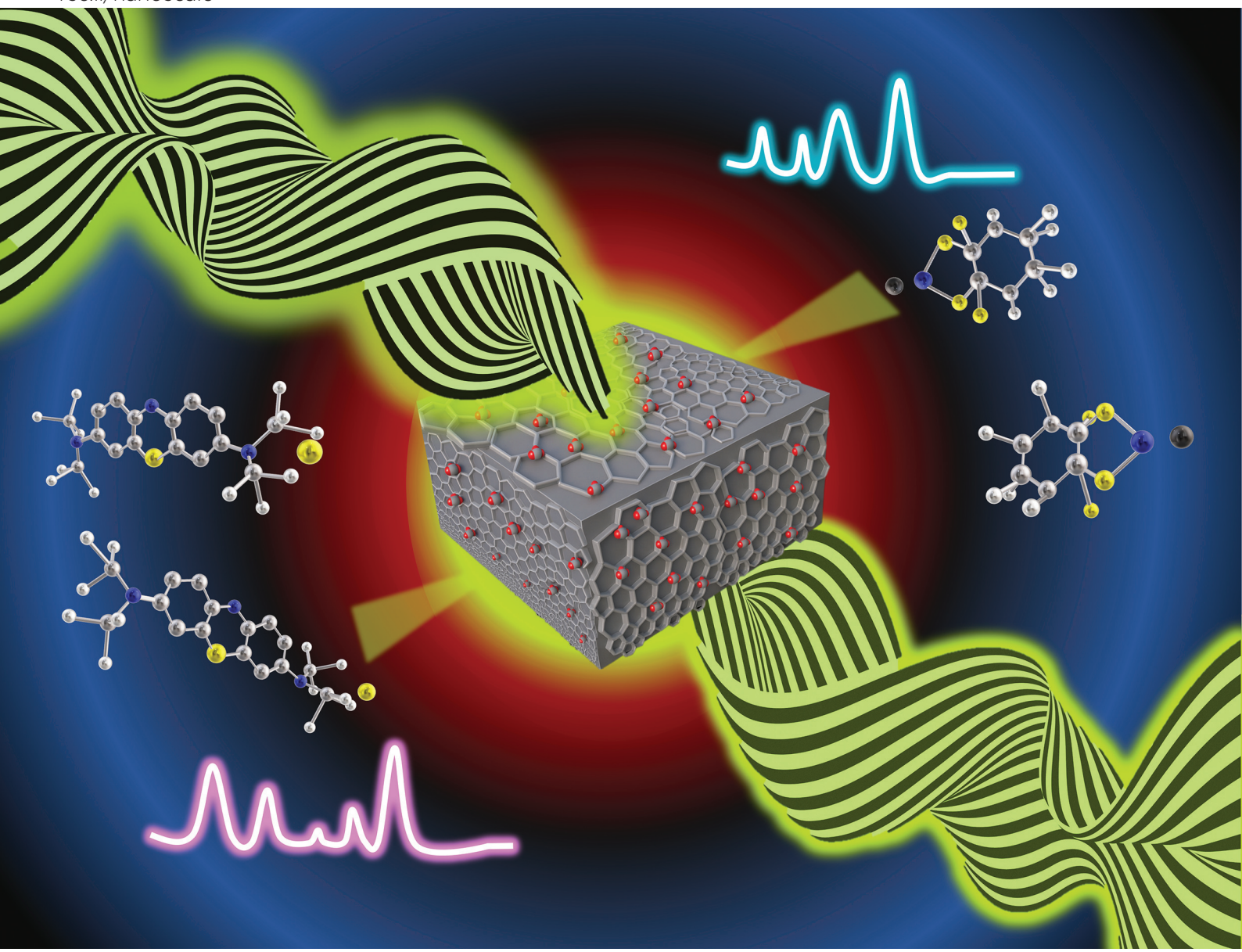

ISSN 2040-3372

PAPER

Shatabdi Porel Mukherjee *et al.*

One-step microwave-assisted synthesis of a MoO_{3-x}-covalent organic framework (COF)-based nanocomposite for amplified surface-enhanced Raman spectroscopy in environmental applications

ROYAL SOCIETY OF CHEMISTRY

NCNST

Nanoscale

PAPER

View Article Online
View Journal | View Issue

Cite this: *Nanoscale*, 2026, **18**, 1345

One-step microwave-assisted synthesis of a MoO_{3-x}-covalent organic framework (COF)-based nanocomposite for amplified surface-enhanced Raman spectroscopy in environmental applications

Manoj Krishnat Patil, [a,b] Premjeet Gangadhar Wagh [a,b] and Shatabdi Porel Mukherjee *[a,b]

This study introduces a novel one-step microwave-assisted (MW-AT) synthesis strategy for a TpTTA COF and demonstrates the fabrication of a MoO_{3-x}-TpTTA COF-based nanocomposite (NC) for the first time. This method significantly reduces synthesis time (~1 h) while achieving a high yield at a moderate temperature (120 °C). In contrast, traditional solution-based COF synthesis methods may take several days with continuous heating at higher temperatures (≤200 °C). The as-synthesized MoO_{3-x}-COF-based NC was shown to serve as an affordable and straightforward substrate for surface-enhanced Raman scattering (SERS) detection of an organic dye, such as methylene blue (MB), achieving a maximum enhancement factor (EF) of 7.76×10^4. The incorporation of MoO_{3-x} into the COF provides several advantages, including plasmonic enhancement by nonstoichiometric transition metal oxide (TMO) without requiring the addition of noble nanocrystals (*e.g.*, Ag, Au, *etc.*), improved stability of the SERS substrate, comparable SERS sensitivity, and reduced costs. Furthermore, the as-synthesized MoO_{3-x}-TpTTA COF-based SERS substrate demonstrated exceptional detection capabilities with high reproducibility, achieving a limit of detection (LOD) as low as 12.5 ppm for Mancozeb (Mz), a common commercially used dithiocarbamate insecticide used on various vegetables, fruits, nuts, and field crops. Notably, Mz is classified as a category III carcinogen by the International Agency for Research on Cancer. This highlights the potential for developing TMO-COF-based NCs for next-generation SERS-based applications in environmental and food safety monitoring.

Received 6th July 2025,
Accepted 4th November 2025

DOI: 10.1039/d5nr02849c

rsc.li/nanoscale

1. Introduction

Covalent organic frameworks (COFs) are crystalline, porous, periodic structures that are specially composed of organic monomers bearing light elements (C, B, N, O, and H) and connected by strong covalent bonds.[1] COFs are an emerging class of materials that demonstrate high chemical stability, high surface area, tunable pore size, and functional tunability.[1,2] Eventually, several solution- and solid state-based COF synthesis procedures are available,[1,3] and they have shown promising applications in catalysis, sensing, adsorption, and optoelectronics.[4–7] Based on their specific framework structure, COFs have been proven to be suitable scaffolds for stabilizing plasmonic metal nanoparticles (NPs), and hence work as efficient SERS substrates with more SERS-active "hot spots".[8] Furthermore, the uniform pores, functionalizable pore interiors, and high surface areas of COFs can also effectively enrich the adsorption of target molecules and lower the detection limit in SERS studies.[8,9] Hence, new explorations are in great demand to develop novel COF-based SERS substrates for highly sensitive and reproducible SERS analysis.[8–10]

The nitrogen-rich triazine-containing TpTTA COF synthesized from Tp (2,4,6-trihydroxybenzene-1,3,5-tricarbaldehyde) and TTA [4,4′,4″-(1,3,5-triazine-2,4,6-triyl)trianiline] is a very promising organic material that is generally synthesized over several days using relatively high-temperature solution-based methods, *e.g.*, sealed tube,[11] solvothermal,[12–19] hydrothermal,[20,21] organic reflux,[21–25] interfacial polymerization,[26,27] self-standing film/membrane,[27–29] seed-mediated strategy,[30] *etc.* The as-synthesized pristine TpTTA COF has shown applications in adsorption,[20] size-selective NP separation,[28,29] solvent filtration,[26] removal of environmental pollutants,[13,27] gas separation,[14] heterogeneous catalysis,[12,15,25] fuel cells,[22,23] Li-ion batteries,[18] *etc.*, whereas the metal or metal NP/TpTTA composite materials show applications in photocatalytic H_2 generation,[15–17,19] photocatalytic CO_2 reduction,[24,30,31] fuel cells,[23] *etc.*

[a]*Physical and Materials Chemistry Division, CSIR-National Chemical Laboratory, Dr Homi Bhabha Road, Pune, 411008, India. E-mail: sp.mukherjee.ncl@csir.res.in*
[b]*Academy of Scientific and Innovative Research (AcSIR), Ghaziabad-201002, India*

However, in this study, for the first time, we report the synthesis of the TpTTA COF using a rapid one-step MW-AT synthesis procedure with significantly less time and high yield at a relatively low temperature. The as-synthesized TpTTA COF exhibits a 2D layered structure with high crystallinity, stability, and BET surface area, as confirmed through various characterization techniques. Since the TpTTA COF bears a large number of *N*,*O*-chelating sites, we could successfully anchor MoO_{3-x} NPs into the channels of this COF, and a modified COF composite, namely, the MoO_{3-x}-TpTTA COF nanocomposite (NC), was also obtained by the rapid one-step MW-AT synthesis method.

Although there are several reports of plasmonic noble metal NP-COF composites for sensitive SERS detection of target molecules, including organic dyes,[8] pesticides,[9] DNA bases,[32] polyaromatic hydrocarbons,[10] SARS-CoV-2 spike protein,[33] *etc.*, to the best of our knowledge, this is the first report where a nonstoichiometric transition metal oxide-COF NC (MoO_{3-x}-TpTTA) is used as the SERS substrate for the sensitive detection studies of organic molecules. As previously reported by our group, in the case of nonstoichiometric metal oxide nanomaterials (NMs),[34–39] including their SERS properties,[38,39] this synthesis strategy is entirely different and has several advantages. Herein, it is a one-step, rapid, novel microwave-based synthesis method and requires no surfactant, stabilizing or reducing agent, inert atmosphere or external pressure.

In addition, to demonstrate the efficacy of the nonstoichiometric metal oxide-COF nanocomposite SERS substrate, we employed the as-synthesized MoO_{3-x}-TpTTA COF NC for sensitive detection of methylene blue (MB), an organic dye. Herein, the nanocomposite exhibited SERS activity with a maximum EF of up to 7.76×10^4, a detection limit as low as 1.0×10^{-7} M and an RSD of 6.10% for SERS reproducibility. Moreover, the NC was further employed to detect trace amounts of Mancozeb (Mz), a common commercially used dithiocarbamate insecticide[40] widely applied in the cultivation of crops such as rice and grapes, which has been classified as a category III carcinogen by the International Agency for Research on Cancer.[40] Although Mz effectively protects crops from fungal infections, its excessive application poses severe risks to human health due to residue accumulation.[41] Therefore, it ought to be of great significance to develop a fast, sensitive, accurate, and effective method to analyze and detect low concentrations of Mz as a model analyte to evaluate the SERS activity and extend the practical applications of the as-synthesized MoO_{3-x}-COF NC-based system. To the best of our knowledge, this is the first report to showcase an ultralow detection capability of a nonstoichiometric TMO-COF nanocomposite, *i.e.*, an MoO_{3-x}-TpTTA-based SERS substrate, with high reproducibility and an LOD of 12.5 ppm for Mz.

2. Experimental section

2.1 Materials

Ammonium heptamolybdate tetrahydrate [AHM, $(NH_4)_2Mo_7O_{24}\cdot 4H_2O$, Loba Chemie, 99.3%, AR/ACS], 2,4,6-trihydroxybenzene-1,3,5-tricarbaldehyde [Tp, Hygeia Laboratories, >97.0%], 4,4′,4″-(1,3,5-triazine-2,4,6-triyl)trianiline [TTA, BLD Pharmatech, 95%], glacial acetic acid [Loba Chemie, 99.7%, AR], 1,4-dioxane [SRL, 99.5% extra pure AR], tetrahydrofuran [THF, SRL, 99.5%, extra pure AR/ACS], mesitylene [Hyma Synthesis, formerly Avra Synthesis, 98%], ethyl alcohol [absolute EtOH, Northman Specialty Chemicals, 99.9%, AR], isopropyl alcohol [IPA, Finar Chemicals, 99.0%, extra pure], MB (Sigma-Aldrich, ≥95%), and fungicide [All Care, Alert Crop Sciences Pvt. Ltd, Mancozeb 63% WP+ Carbendazim 12% WP] were used as received. Mesitylene, THF and IPA were used as the solvents.

2.2 Material preparation

2.2.1 Synthesis of the TpTTA COF. The synthesis of the TpTTA COF was initiated by dispersing 159 mg (0.45 mmol) of TTA in a G30 glass vial of an Anton Paar Monowave 300 microwave reactor, followed by the addition of 0.5 mL of 3 M acetic acid to ensure complete ionization of the amine groups. Next, 64 mg (0.3 mmol) of Tp was added, and the mixture was homogenized by introducing 5 mL of a 1 : 1 solvent blend of 1,4-dioxane and mesitylene, followed by brief stirring with a magnetic rod. The remaining 10 mL of solvent was added, and the vial was sealed before being subjected to microwave heating at 120 °C for 1 hour in an Anton Paar Monowave 300 reactor. The reactor initially operated at a maximum power of approximately 240–250 W to reach the target reaction temperature of 120 °C. Once this temperature was achieved, the power stabilized at around 20–30 W to maintain the set temperature. The maximum internal pressure recorded during the reaction ranged from approximately 3 to 4 bar. The TpTTA COF was then purified through sequential washes with mesitylene, THF, and IPA using sonication and centrifugation at 10 000 rpm, followed by drying in a vacuum oven at 80 °C for 12 hours to yield highly crystalline frameworks suitable for advanced applications.

2.2.2 Synthesis of the MoO_{3-x}-TpTTA COF NC. For the synthesis of the MoO_{3-x}-TpTTA COF NC, 100 mg of AHM, dissolved in 2.5 mL of water, was added to the reaction mixture after the Tp component, maintaining identical reaction conditions as the TpTTA COF. The resulting MoO_{3-x}-TpTTA COF NC was purified in the same manner, with sequential washes in mesitylene, THF and IPA, sonication and centrifugation at 10 000 rpm, followed by drying at 80 °C in a vacuum oven for 12 hours, yielding a highly crystalline framework.

2.3 Material characterization

The wide-angle X-ray diffraction (WAXD) analysis was recorded on a Rigaku MicroMax 007HF equipped with a high-intensity microfocus rotating anode X-ray generator. The data were collected with the help of Control Win software. A Rigaku *R*-axis IV++ detector was used for the wide-angle experiments using Cu K-alpha (1.54 Å) radiation outfitted with a Ni filter, and an aluminium holder was used as the sample holder. The microscopic morphologies of the as-synthesized products were obtained using a field emission scanning electron microscope (FEI NOVA NANOSEM 450) at an acceleration voltage of 0.5–30 kV. High resolution transmission electron microscopy (JEOL,

JEM F200 with an accelerating voltage of 200 keV) equipped with energy dispersive spectroscopy (EDS), high-angle annular dark-field scanning transmission electron microscopy and selected area electron diffraction (SAED) was used. The optical properties of the samples were characterized by UV-vis spectra over 300–1000 nm, taken on a Shimadzu UV-3600 Plus spectrometer using $BaSO_4$ as the reference. Fourier transform infrared (FT-IR) spectra were recorded using a PerkinElmer Spectrum 3 (attenuated total reflection) accessory in the 600–4000 cm^{-1} region. The valence state and elemental composition of the products were analyzed by X-ray photoelectron spectroscopy (Thermo Scientific Kα+) equipped with a monochromatic Al Kα X-ray (50 eV) source. All XPS spectra were calibrated with charge correction, referenced to the C 1s peak at 284.8 eV. Thermogravimetric analysis (TGA) of the samples was carried out in a PerkinElmer STA 600 analyzer under an N_2 atmosphere by maintaining a temperature ramp between room temperature and 900 °C with a heating rate of 10 °C min. A Brunauer–Emmett–Teller (BET) adsorption experiment (up to 1 bar) of COF samples was performed on a Quantachrome Autosorb-iQ2 gas sorption analyzer. Before surface area analysis, the samples were activated at 120 °C for 8 hours. The porosity of samples was measured by N_2 adsorption of an activated sample at 77 K. The average pore diameter of the samples was calculated by nonlocal density functional theory (NLDFT). The BET surface area of the samples was determined by Multipoint BET analysis. The electron paramagnetic resonance (EPR) spectra were recorded on an EMX plus spectrometer at X-band (9.5 GHz) frequency. The solid-state NMR ^{13}C spectrum was recorded on a Bruker AV Neo 500 with a 14 kHz spinning frequency. The Raman measurement was performed on a Technos IndiRAM CTR-500 Micro Raman Spectrometer using a 532 nm diode laser. The inductively coupled plasma optical emission spectroscopy (ICP-OES) analysis was performed on the Spectro Acros FHS1 instrument, calibrated at Mo 10 ppm using Sigma Aldrich ICP multielement standard II.

2.4 SERS measurements

2.4.1. SERS measurements for analyte MB. MB was used as the target molecule to examine the Raman enhancement effect of the MoO_{3-x}-TpTTA COF NC. Ethanol solutions of MB ranging from 10^{-1} to 10^{-7} M were prepared. 2 mg of the MoO_{3-x}-TpTTA COF NC substrate was added to 10 mL of MB solutions of different concentrations, and the mixture was allowed to equilibrate for 8 h with constant stirring at 450 rpm in the dark. The MoO_{3-x}-TpTTA COF NC substrates loaded with MB were collected by centrifugation, followed by overnight drying in a vacuum desiccator. The SERS measurements were carried out using an IndiRAM CTR-500 Raman spectrometer with a 532 nm laser excitation source operating at 1 mW power, focused through 50× and 100× objectives to produce spot diameters of 1.5 μm and 0.5 μm, respectively. Each sample was analyzed with an integration time of 5–8 seconds, and triplicate measurements were performed to ensure statistical reliability. The SERS EFs were calculated using the standard equation as previously reported by our group.[38,39]

To address the potential impact of COF decomposition on SERS signal stability under laser heating, the temperature increase during laser irradiation was measured using an IR thermometer with the same laser exposure parameters applied during SERS analysis. It was found that the temperature of the SERS substrate did not exceed room temperature (approximately 22–24 °C), as the SERS analysis was carried out with a laser power of 1 mW and an integration time of 5–8 seconds. The SERS substrate remained thermally stable throughout the Raman measurements, and no adverse effects were observed in the SERS analysis.

2.4.2. SERS measurements for the commercial fungicide. The fungicide Mz was dissolved in ethanol to prepare a series of standard solutions with concentrations ranging from 2000 ppm to 12.5 ppm. For sample preparation, precisely 2 mg of the synthesized COF composite or COF substrate was dispersed in 10 mL of each fungicide solution in a 25 mL beaker, and the mixtures were equilibrated under dark conditions with continuous stirring for 8 hours to ensure maximal adsorption. Post-equilibration, the fungicide-loaded COF composite and COF substrates were isolated by centrifugation and dried under vacuum overnight. Raman spectra were acquired using an IndiRAM CTR-500 Raman spectrometer under similar conditions used for MB detection. Control experiments were conducted to compare the performance of only the TpTTA COF and MoO_{3-x}-TpTTA COF NC substrates.

2.4.3. SERS reproducibility measurements. A 1×10^{-4} M MB solution was used to verify the uniformity of the SERS signal obtained from the MoO_{3-x}-TpTTA COF NC substrate. A total of 10 measuring points were randomly selected from the SERS substrate to record the SERS enhancement, and the relative standard deviation (RSD) was calculated for the characteristic MB peak at 1624 cm^{-1}.[39]

2.4.4. Long-term storage stability and reusability of the SERS substrate. The sample was prepared by following the guidelines in section 2.4.2 and was used to examine SERS detection of 500 ppm Mz over a four-week period, with assessments conducted every two weeks. The sample was stored in a vacuum desiccator throughout the study.

3. Results and discussion

3.1 Synthesis of the TpTTA COF and MoO_{3-x}-TpTTA COF NC

COFs are highly versatile materials with tunable structures, achieved by modifying their organic monomers; however, attaining high crystallinity and porosity remains a formidable challenge. Strategies to enhance these properties include improving interlayer interactions through hydrogen bonding, reinforcing π–π stacking to stabilize the framework, and optimizing synthesis methodologies.[42] Among these, MW-AT synthesis has emerged as a transformative approach, promoting cleaner and more sustainable synthesis pathways for COF fabrication, offering rapid reaction times, higher reaction rates, uniform heating, enhanced product yields, and energy efficiency.[43] However, limited studies have explored this

method; for example, Wei *et al.* demonstrated two-dimensional enamine-linked COF synthesis using an MW-AT solvothermal method at 100 °C within 1 h under a nitrogen atmosphere,[44] while triazine-based COFs, known for their exceptional stability and extended π-conjugation, have been primarily synthesized *via* relatively slower methods, such as refluxing anhydrous solvent at 150 °C for 12 h under an inert atmosphere, as reported by Gomes *et al.*[45] To bridge the synthesis gap, we have developed a rapid and efficient MW-AT synthesis strategy for the enamine-linked nitrogen-rich triazine-containing COF synthesized with Tp and TTA, named the TpTTA COF, achieving highly crystalline and porous frameworks within 60 minutes, as shown in Fig. 1. Following the same reaction protocol, by addition of an ammonium heptamolybdate (AHM)/water mixture to the Tp and TTA mixture, the nonstoichiometric metal oxide-COF *i.e.* the MoO_{3-x}-TpTTA NC has been synthesised *via* the MW-AT synthesis strategy (Fig. 1).

The powder X-ray diffraction (PXRD) measurements confirm the formation of a crystalline framework of the TpTTA COF (Fig. 2a). The PXRD patterns of the TpTTA COF are consistent with the previous report, exhibiting well-defined diffraction peaks at 2θ values of 5.96°, 9.92°, 15.34°, and 26.69°, corresponding to the (100), (110), (210), and (001) crystallographic planes, respectively, indicative of a highly ordered and crystalline framework.[12,20] Similarly, the MoO_{3-x}-TpTTA COF displayed characteristic peaks at 2θ values of 5.59°, 9.89°, 15.13°, and 26.53° assigned to the same reflection planes, albeit with slight shifts attributable to the incorporation of MoO_{3-x} species in the COF nanocomposite (Fig. 2a). However, no regular diffraction peaks associated with crystalline MoO_{3-x} were observed, which may be due to the low concentration of MoO_{3-x} inside the COF nanocomposite or MoO_{3-x} species are homogeneously embedded within the COF matrix.[16]

The TpTTA COF and the MoO_{3-x}-TpTTA COF NC samples were investigated by UV-Vis absorption spectroscopy, as shown in Fig. 2b. The TpTTA COF showed UV-Vis absorption around 316, 380, and 579 nm, whereas a significant increase in the

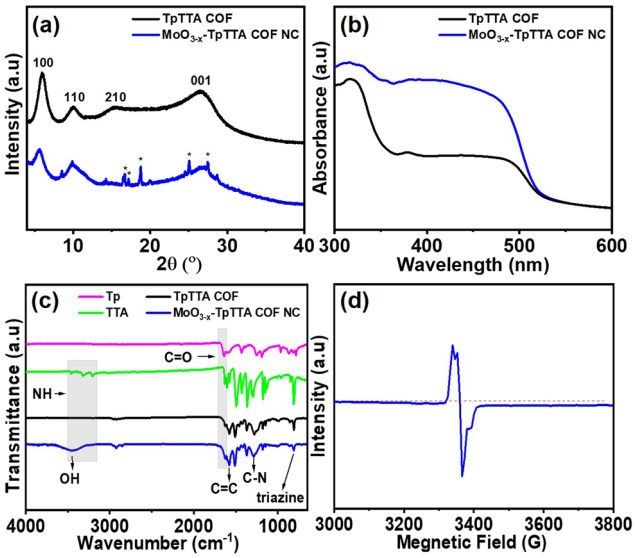

Fig. 2 (a) PXRD pattern, (b) UV-Vis spectrum, (c) FT-IR spectrum of the TpTTA COF and MoO_{3-x}-TpTTA COF NC, and (d) the EPR spectrum of the MoO_{3-x}-TpTTA COF NC.

absorption band spanning the 380–520 nm region was observed in the absorption spectra of the MoO_{3-x}-TpTTA COF NC, along with the peaks obtained for the TpTTA COF. Generally, MoO_{3-x} showed a strong absorption peak centered around 700 nm, mostly associated with localized surface plasmon resonance (LSPR) due to the presence of a significant amount of free carriers related to oxygen vacancies.[38] However, due to overlap with the absorption spectra in the UV region of the TpTTA COF, the presence of the absorption peak associated with the LSPR properties of MoO_{3-x} in the MoO_{3-x}-TpTTA COF NC cannot be concluded.

The Fourier-transform infrared (FTIR) spectra of the TpTTA COF and MoO_{3-x}-TpTTA COF NC are depicted in Fig. 2c. The disappearance of the C═O stretching bands of Tp and N–H

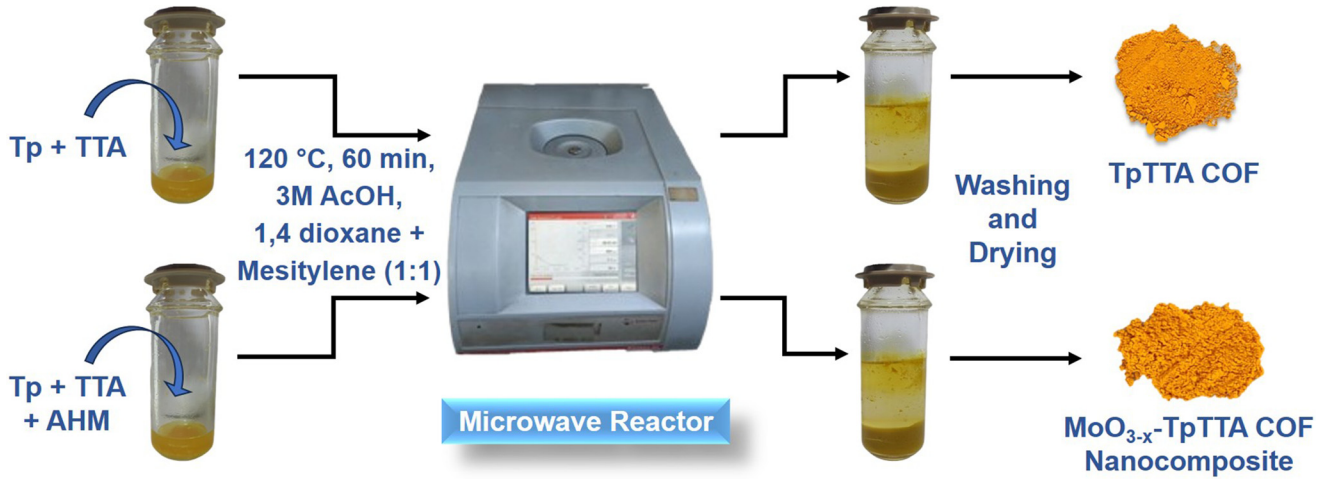

Fig. 1 Schematic illustration of one-step MW-AT synthesis of the TpTTA COF and MoO_{3-x}-TpTTA NC.

stretching bands of TTA provided direct evidence for TpTTA COF formation.[12,13] The TpTTA COF exhibited distinct absorption bands at 1580, 1285 and 810 cm^{-1} resulting from the C=C stretching, C–N stretching, =C–H in-plane bending, and triazine group, which are characteristic of an enamine-linked framework formed *via* a Schiff-base condensation reaction.[12,16] In addition, the dominant peak at 1580 cm^{-1} resulting from the C=C stretching and the lack of O–H and –NH stretching demonstrate that the TpTTA COF existed in the keto form. The FTIR spectra of the MoO_{3-x}-TpTTA COF NC reveal the retention of characteristic vibrational features, albeit with minor shifts (Fig. 2c). Notably, the emergence of a broad absorption band at 3446 cm^{-1}, attributed to O–H stretching vibrations, provides compelling evidence that the TpTTA COF exists in its enol tautomeric form when integrated with MoO_{3-x} in the nanocomposite. This phenomenon is particularly remarkable, as it is hardly observed in studies involving COFs and COF-based nanocomposites.

The electron paramagnetic resonance (EPR) analysis of the MoO_{3-x}-TpTTA COF NC revealed significant insights, as illustrated in Fig. 2d. A distinct isotropic signal with $g \approx 2.04$, characteristic of Mo^{5+} centers. The observed narrow peak-to-peak separation indicates the presence of well-defined, stable radical species. The absence of hyperfine splitting suggests that the unpaired electron is delocalized across the molecular framework rather than localized on a single atom. This finding compellingly underscores the existence of oxygen vacancies and highlights the nonstoichiometric characteristics of molybdenum oxide within the MoO_{3-x}-TpTTA COF NC sample.[46]

The chemical composition and elemental chemical states of the TpTTA COF and MoO_{3-x}-TpTTA COF NC samples were analyzed through X-ray photoelectron spectroscopy (XPS). The XPS survey spectra of the TpTTA COF and MoO_{3-x}-TpTTA COF NC are represented in Fig. S1a and b, respectively (see the SI). Three prominent binding energy peaks at 284.58 eV (C 1s), 398.58 eV (N 1s), and 531.58 eV (O 1s) were observed for the TpTTA COF,[16,21] and four prominent binding energy peaks at 232.41 eV (Mo 3d), 284.41 eV (C 1s), 398.41 eV (N 1s), and 531.41 eV (O 1s) were observed for the MoO_{3-x}-TpTTA COF NC.[16,38] For the as-synthesized TpTTA COF, the high-resolution deconvolution of the C 1s spectrum revealed distinct peaks located at 283.88, 285.48, and 289.08 eV were assigned to C=C, C=N–C, and C=O, respectively, affirming the integrity of the conjugated structure (Fig. 3a).[16] The N 1s spectrum displayed well-resolved peaks corresponding to C=N–C at 397.78 eV, C=N at 399.28 eV, and chemisorbed N–H at 402.38 eV, indicating the electronic environment of nitrogen from the triazine center within the enamine-linked COF network (Fig. 3b).[16] Similarly, the O 1s spectra indicated C=O at 530.28 eV, –OH at 532.28 eV, and chemisorbed H_2O at 534.78 eV, confirming the presence of oxygen functionalities integral to the COF architecture (Fig. 3c).[30] On the other hand, for the MoO_{3-x}-TpTTA COF NC, the Mo 3d XPS spectrum showed two peaks that can be fitted by two pairs of doublets, which correspond to a mixed-valence state of molybdenum oxide nanostructures (Fig. 3d). The characteristic peaks located at 236.41 and 233.41 eV were assigned to Mo^{6+}, and those at 235.41 and 232.41 eV correspond to Mo^{5+} for the MoO_{3-x}-TpTTA COF NC sample (Fig. 3d).[38,47] In comparison with the graphics present in Fig. 3d, Table S1 (see the SI) provides the calculated percentages of Mo^{6+} and Mo^{5+} in the MoO_{3-x}-TpTTA COF NC sample using CasaXPS software. The analysis revealed that the percentages of Mo^{6+} and Mo^{5+} were 80.92% and 19.07%, respectively. The presence of low-valent Mo^{5+} in the lattice is attributed to the formation of oxygen vacancies, which help to balance the overall charge. This finding further confirms the nonstoichiometric characteristics of the molybdenum oxide within the MoO_{3-x}-TpTTA COF NC sample. In addition, the high-resolu-

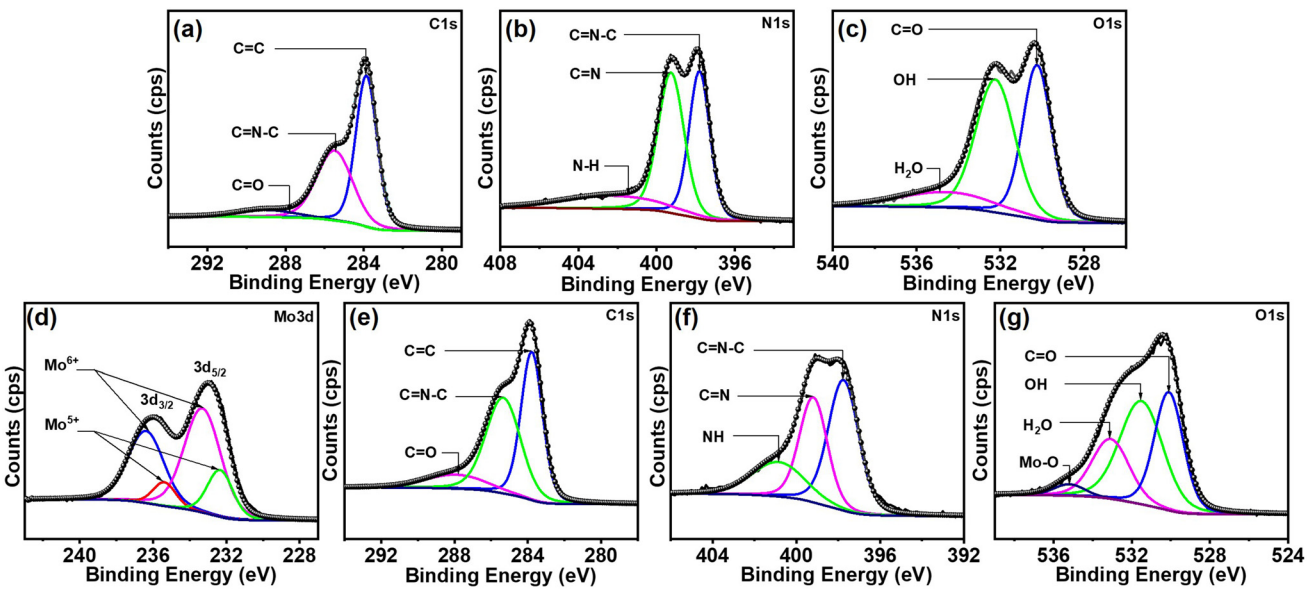

Fig. 3 XPS spectra of the TpTTA COF: (a) C 1s, (b) N 1s, (c) O 1s and the MoO_{3-x}-TpTTA COF NC: (d) Mo 3d, (e) C 1s, (f) N 1s, and (g) O 1s.

tion C 1s spectra exhibit characteristic peaks corresponding to C═C at 283.81 eV, C═N–C at 285.41 eV, and C═O at 288.01 eV (Fig. 3e).[16] The N 1s spectrum displays distinct peaks attributed to C═N–C at 397.81 eV, C═N at 399.21 eV, and chemisorbed N–H at 400.91 eV (Fig. 3f),[16] and the O 1s spectrum indicated C═O at 530.11 eV, –OH at 531.51 eV, chemisorbed H_2O at 533.11 eV, and Mo–O at 535.21 eV (Fig. 3g).[30] These results were in good agreement with the EPR analysis, proving the presence of free electrons, which can localize to form Mo^{5+} centres and suggest the existence of oxygen-deficient MoO_{3-x} within the COF moiety for the MoO_{3-x}-TpTTA COF NC sample.[46]

The N_2 adsorption–desorption isotherm of the MoO_{3-x}-TpTTA COF NC exhibited a decrease in the Brunauer–Emmett–Teller (BET) surface area for the MoO_{3-x}–TpTTA COF NC (110.3 $m^2\ g^{-1}$) compared to the pristine COF (122.8 $m^2\ g^{-1}$). This reduction can be attributed to the encapsulation of the MoO_{3-x} moiety within the porous structure of the TpTTA COF (Fig. S2, SI).[16,48] The DFT pore size distribution analysis indicated that the average pore size for both the pristine TpTTA COF and the MoO_{3-x}–TpTTA COF NC remained in the range of ~1.5 nm, suggesting that there was no significant change in pore size distribution upon the incorporation of the MoO_{3-x} moiety into the TpTTA COF matrix (Fig. S3a and b, SI).[48] Both the COF and COF nanocomposite showed a type-IV isotherm with a hysteresis loop, which is fully consistent with the reported literature.[16,48]

Thermogravimetric analysis (TGA) elucidates the thermal stability and decomposition behavior of the TpTTA COF and the MoO_{3-x}-TpTTA COF NC, revealing distinct degradation pathways influenced by the incorporation of MoO_{3-x}, as shown in Fig. S4 (see the SI). The pristine TpTTA COF exhibits excellent thermal stability, with an initial weight loss around 150 °C, attributed to the removal of the trapped solvents in the MoO_{3-x}-TpTTA COF NC. The framework remains structurally intact up to 450 °C, experiencing only a 21% weight loss, indicative of the strong covalent enamine linkages within the COF backbone. Beyond this threshold, gradual decomposition occurs, followed by the formation of thermally resilient carbonaceous residues, with 63% of the initial mass retained at 800 °C, suggesting partial graphitization.[12] Conversely, the MoO_{3-x}-TpTTA COF NC undergoes a continuous, progressive weight loss (~11%) up to 370 °C, followed by a sharp decomposition at 390 °C, indicative of framework destabilization, culminating in a major 78% weight loss at 470 °C, signifying the collapse of the organic backbone.[23] This accelerated decomposition is attributed to the incorporation of MoO_{3-x}, which introduces localized charge delocalization and free-electron density, thereby weakening the imine linkages and facilitating premature thermal degradation. The material undergoes near-total decomposition by 800 °C, highlighting the catalytic influence of MoO_{3-x} on thermal breakdown mechanisms.[49] The ICP-OES analysis was performed to determine the Mo loading percentage in the COF matrix, which was found to be 0.5 wt%. This experiment suggested a low Mo loading in the MoO_{3-x}-TpTTA COF NC.

The solid-state ^{13}C NMR analysis of the TpTTA COF and MoO_{3-x}-TpTTA COF NC reveals distinct changes in the electronic environment of the framework due to the incorporation of the MoO_{3-x} moiety. For the TpTTA COF, the characteristic peaks of C═O, C═N and C═C appear at 184.96 ppm, 169.35 ppm and 107.67 ppm, respectively (Fig. S5a, SI), while for the MoO_{3-x}-TpTTA COF NC, minor shifts were observed at 184.19 ppm, 168.61 ppm and 107.50 ppm, respectively (Fig. S5b, SI).[26,28] These chemical shifts are further attributed to the successful integration of MoO_{3-x}, which alters the electronic properties of the TpTTA COF in the MoO_{3-x}-TpTTA COF NC due to its paramagnetic nature as confirmed by EPR and XPS analyses.[50]

The morphological characterization of the TpTTA COF and MoO_{3-x}-TpTTA COF NC was performed through FESEM and HRTEM analyses. The FESEM images showed that the synthesized TpTTA COF exhibited a fibrous morphology (Fig. S6a, SI) and maintained the same morphology after incorporating the MoO_{3-x} moiety into the COF (Fig. 4a). As displayed in the HRTEM images, the TpTTA COF shows lamellar stacking structures (Fig. S6b, SI), whereas encapsulated MoO_{3-x} NPs of size ~7–9 nm were observed in the HRTEM image of the MoO_{3-x}-TpTTA COF NC sample, as shown in Fig. 4c. The majority of the NPs are spherical in shape. The particle size distribution histogram was created based on the NPs observed in the HRTEM images and is presented in the inset of Fig. 4(c). However, due to the low molybdenum loading (0.5 ppm) in the MoO_{3-x}-TpTTA COF NC, the number of NPs in the COF matrix is too low to accurately calculate the mean particle size and its standard deviation. The *d*-spacing value observed for MoO_3 NPs was 0.17 nm.[51] This indicated that the MoO_{3-x} NPs are homogeneously integrated within the COF at the nanoscale, ensuring consistent and stable loading. This integration preserves the intrinsic crystallinity of the COF, ensuring both its structural integrity and uniform functionalization.[16,19] The EDS elemental analysis (Fig. 4b and inset table), the high-

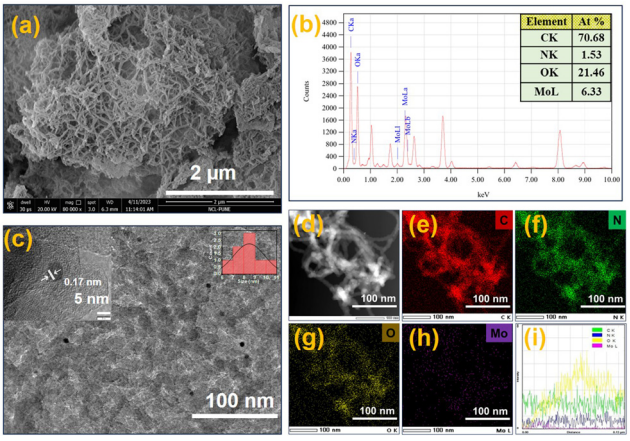

Fig. 4 (a) FESEM, (b) EDS, and (c) HRTEM images; the inset shows fringes and the particle size distribution histogram of MoO_{3-x} NPs; (d) HAADF-STEM image, (e)–(h) elemental mapping and (i) line mapping of the MoO_{3-x}-TpTTA COF NC.

angle annular electron microscopy (HAADF-STEM) image (Fig. 4d), elemental mappings (Fig. 4e–h) and the line mapping profile (Fig. 4i) of the MoO_{3-x}-TpTTA COF NC revealed the presence of Mo, C, N, and O, supporting the encapsulation and uniform distribution of MoO_{3-x} inside the TpTTA COF nanocomposite.[16] In comparison, the EDS analysis and elemental mapping of the TpTTA COF confirmed the presence of only C, N, and O (Fig. S6c and the inset table and Fig. S6d–g, SI).[18] These findings unequivocally demonstrate the successful incorporation of MoO_{3-x} NPs into the COF, achieving a uniform nanoscale dispersion that preserves the structural integrity of the COF and ensures the effective integration of active sites for enhanced performance in advanced applications.[16,19]

To evaluate the efficiency of our proposed one-step MW-AT synthesis strategy for the fabrication of the MoO_{3-x}-TpTTA COF-based NC, a two-step MW-AT synthesis of the nanocomposite material was conducted. In this process, AHM was added after the formation of the TpTTA COF. In this two-step synthesis, the COF and the aqueous medium formed two distinct layers, as shown in Fig. S7b (see the SI). This separation was absent in the one-step microwave-assisted synthesis, as illustrated in Fig. S7a (see the SI). Moreover, the colours of the products differ significantly between the two methods, as depicted in Fig. S7a and b (see the SI). The introduction of AHM after COF formation led to the production of large and irregularly sized molybdenum oxide nano/microrods, as confirmed by the TEM analysis of the as-synthesized product shown in Fig. S7c (see the SI).

Based on the above results, the schematic illustration of the structure formation in the case of the TpTTA COF and MoO_{3-x}-TpTTA COF NC is shown in Fig. 5. Thus, the synthesis of the TpTTA COF is based on the Schiff base condensation reaction, wherein imine (–C═N–) linkages are formed through the reaction between Tp and TTA.[12–30] The reaction proceeds *via* a keto–enol tautomerization pathway, ultimately stabilizing in the thermodynamically favourable keto form of the TpTTA COF upon completion of the reaction.[12–30] In addition, the synthesis of the MoO_{3-x}-TpTTA COF NC follows a similar strategy

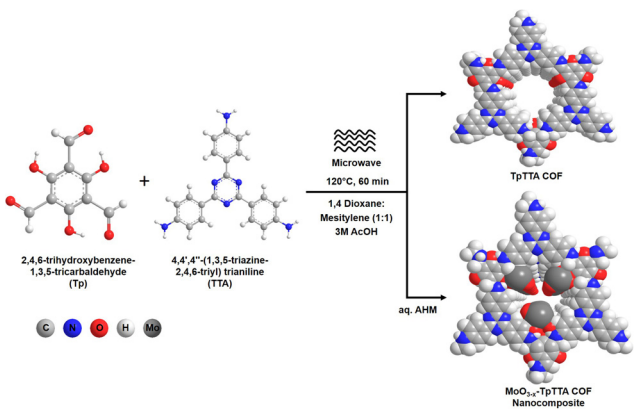

Fig. 5 Schematic illustration of the structure formation of the TpTTA COF and MoO_{3-x}-TpTTA COF NC.

to that of the TpTTA COF, with a slight modification. Under microwave irradiation, the ammonium heptamolybdate decomposes into molybdenum oxide and under a reducing atmosphere, it transforms into MoO_{3-x},[38] anchors onto the COF, and stabilizes the TpTTA COF structure in its enol form, an otherwise challenging state to achieve under standard conditions. In addition, the porous nature of the TpTTA COF effectively restricts the uncontrolled growth of MoO_{3-x}, preventing aggregation and ensuring uniform dispersion. The organic COF plays a crucial role in regulating MoO_{3-x} deposition, leading to a well-integrated MoO_{3-x}-TpTTA COF, which was well-matched with the results obtained from the FTIR, solid-state NMR, EPR, XPS, and HRTEM analyses.[12–30,38,46–51]

3.2 SERS performance of the MoO_{3-x}-TpTTA COF NC

3.2.1. SERS detection of MB. Even though noble metal NMs have been extensively used as SERS-active substrates,[8–10] recently, TMOs, including nonstoichiometric TMOs, also played an essential role in the development of novel SERS-based sensors.[38,39,52,53] Therefore, the nonstoichiometric characteristics of molybdenum oxide within the MoO_{3-x}-TpTTA COF NC enabled us to investigate the possible application of the MoO_{3-x}-TpTTA COF as a SERS substrate for ultrasensitive detection of methylene blue (MB). Fig. 6a demonstrates the typical diagram for the SERS measurements. Additionally, Fig. 6b represents the Raman spectrum of 10^{-1} M pure MB solution, with the most prominent characteristic vibrational peak of MB as 1624 cm^{-1}, which was used for the SERS EF calculation.[38,39] (see experimental section and SI for details). Different concentrations ranging from 1×10^{-1} to 1×10^{-7} M MB solutions were prepared and verified to estimate the sensitivity of the SERS active MoO_{3-x}-TpTTA COF NC, as shown in Fig. 6c. The real images of variable concentrations of MB analyte solutions are also displayed in Fig. 6(i–vii). The fingerprint Raman band of MB (1624 cm^{-1}) was still noticeable at a low concentration of 1×10^{-7} M (Fig. 6c). The dependence of Raman peak intensity (1624 cm^{-1}) on MB concentration is illustrated in Fig. 6d. The error bars in Fig. 6d specify the standard deviation of the mean values obtained from measurements across nine to ten different areas. The peak intensity at 1624 cm^{-1} exhibited a nearly linear correlation with the MB concentration within the range of 1×10^{-1} to 1×10^{-7} M, with a linear correlation coefficient of 0.79 (Fig. 6e). During the SERS analysis, it was observed that the laser-induced photoluminescence (PL) from the COF nanocomposite partially masked the Raman signals. As the concentration of the target analyte decreased, the substrate displayed stronger PL emissions. This increase in fluorescence background obscured the weak SERS signals and distorted their apparent intensity, resulting in a reduced statistical correlation between the analyte concentration and the observed Raman intensity.[54] Consequently, this led to a slightly lower correlation coefficient of 0.79. However, the MoO_{3-x}-TpTTA COF NC has demonstrated SERS activity with the maximum EF up to 7.76×10^4 (Fig. 6f). The detailed EF calculations are provided in the SI (Table S2).

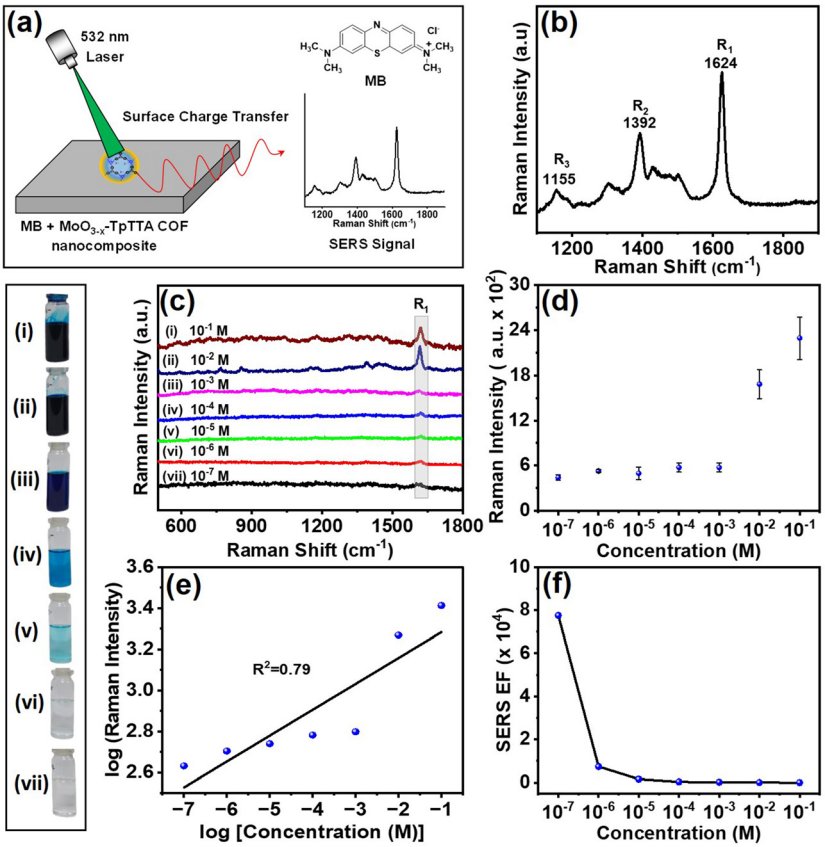

Fig. 6 (a) Schematic diagram of the MoO_{3-x}-TpTTA COF NC as the substrate for SERS detection. (b) Raman spectra of pure MB (10^{-1} M). (c) SERS spectra of MB adsorbed on the surface of the MoO_{3-x}-TpTTA COF NC substrate, with different concentrations in the range of 1×10^{-1} to 1×10^{-7} M; (i–vii) images of varying concentrations of MB solutions (1×10^{-1} to 1×10^{-7} M). (d) Dependence of Raman peak intensity (1624 cm^{-1}) on MB concentration. The error bars show the standard deviation of the mean values of measurements over different areas. (e) A linear relationship between log *I* by selecting the characteristic peak (1624 cm^{-1}) and log *C* based on the SERS data of the MB solutions. (f) Average Raman EF estimated by the characteristic peak (1624 cm^{-1}) of MB with 1×10^{-1} to 1×10^{-7} M concentrations.

3.2.2. SERS reproducibility of the MoO_{3-x}-TpTTA COF NC. The reproducibility of the SERS signal is an additional critical indicator for the practical application of a SERS substrate. The MB solution of 1×10^{-4} M concentration was studied to verify the uniformity of the SERS signal obtained from the MoO_{3-x}-TpTTA COF NC substrate, as displayed in Fig. S8a (see the SI). A total of 10 random measuring points were selected from the MoO_{3-x}-TpTTA COF NC SERS substrate, and the results showed that the obtained SERS signals were mostly dependable. For a characteristic peak at 1624 cm^{-1}, the Raman spectra recorded from 10 points were used to calculate their RSD, as presented in Fig. S8b (see the SI). The calculated RSD was 6.10%, which verified that the measured values determined from a new type of MoO_{3-x}-TpTTA COF NC SERS substrate were well reproducible.[39,55]

3.2.3. SERS detection of Mancozeb (Mz). The as-synthesized MoO_{3-x}-TpTTA COF NC was used as a SERS active substrate to investigate and detect Mz, a common commercially used dithiocarbamate insecticide, which is commonly used on many vegetables, fruits, nuts, and field crops. A systematic and contact commercial fungicide, All Care (Alert Crop Science Pvt. Ltd), containing a combination of Mz (63% WP) and Carbendazim (12% WP) was used herein as the model analyte to study the effectiveness of the as-synthesized MoO_{3-x}-TpTTA COF NC SERS substrate in probable real life applications. The commercial fungicide used in the study contains a high concentration of Mz (~ 63% WP) and has a recommended application limit of 2000 ppm (2 g L^{-1}) for effective use on crops.[56] In order to examine Mz, the standard Raman spectra of Mz at 2000 ppm were collected, as shown in Fig. 7a. The most prominent vibrational peaks of Mz were observed at 1525, 1449 and 1338 cm^{-1} caused by the (C=N) stretching coupled with the deformation (NH) and (CH_2) vibrations and N–H and C–C stretching vibrations.[57,58] Another vibration peak at 1140 cm^{-1} was attributed to the coupling of CH_3 rotational vibration and C–N vibrations.[57,58] The peaks at 840 and 950 cm^{-1} were attributed to the bending vibration of N–H and stretching vibration of C=S, respectively, and the peaks at 680 and 592 cm^{-1} were observed for interaction between Zn, Mn and the C–S–S group.[57,58]

In order to quantitatively analyze Mz, a series of standard solutions with different concentrations from 2000 ppm to

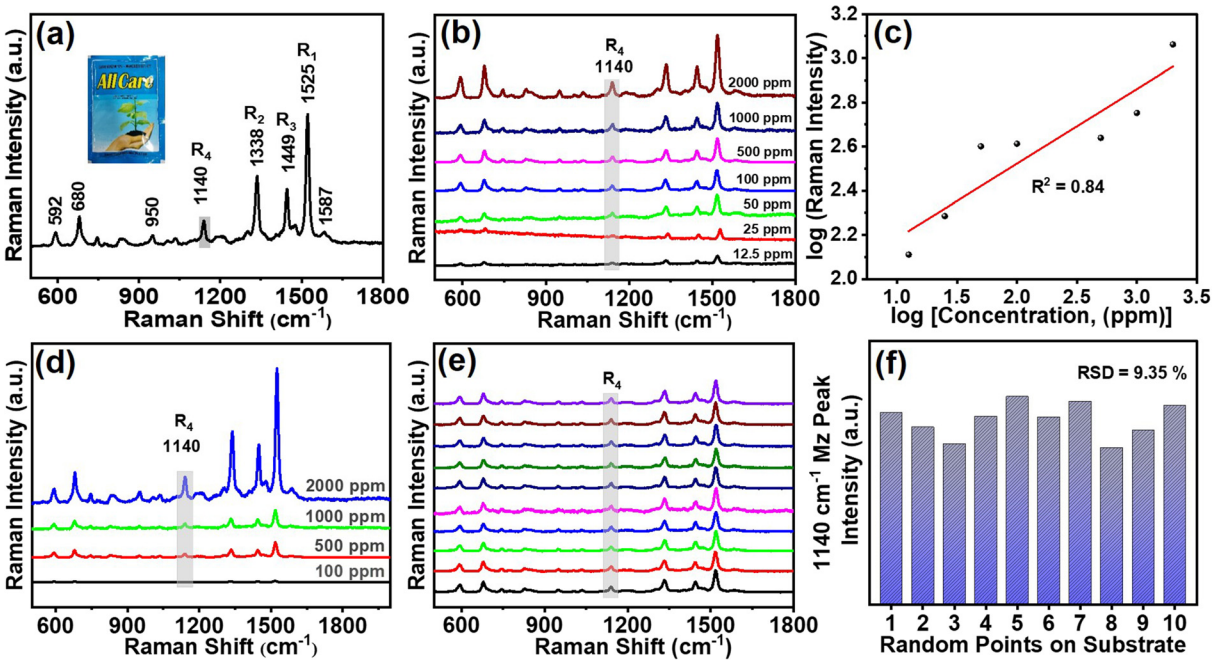

Fig. 7 (a) Raman spectra of Mancozeb (2000 ppm): the inset shows the real image of the commercial packet used in the study. (b) SERS signals of Mancozeb adsorbed on the surface of the MoO_{3-x}-TpTTA COF NC substrate, with different concentrations in the range of 2000 ppm to 12.5 ppm. (c) Linear relationship between log *I* by selecting the characteristic peak (1140 cm^{-1}) and log *C* based on the SERS data of the Mancozeb solutions. (d) Raman spectra of Mancozeb adsorbed on the surface of the TpTTA COF substrate, with different concentrations in the range of 2000 ppm to 100 ppm. (e) SERS spectra of 500 ppm Mancozeb on the MoO_{3-x}-TpTTA COF NC collected from 10 randomly chosen sites on the substrate. (f) The intensity distribution of the 1140 cm^{-1} peak of 500 ppm Mancozeb on the MoO_{3-x}-TpTTA COF NC.

12.5 ppm were investigated to evaluate the sensitivity of the MoO_{3-x}-TpTTA COF NC SERS substrate (Fig. 7b). However, to avoid any ambiguity arising from large wavenumber bands of Mz that partially overlap with the D and G bands of the carbon content in the COF in the MoO_{3-x}-TpTTA COF NC within the range of 1400–1600 cm^{-1}, the characteristic peak of Mz at 1140 cm^{-1} was selected for SERS detection. The fingerprint Raman band at 1140 cm^{-1} was still noticeable at a low concentration of 12.5 ppm (Fig. 7b). It was observed that the intensity of SERS increases with the increase of Mz concentration. As revealed in Fig. 7c, the standard curve showed linearity in the range from 12.5 to 2000 ppm, with a linear correlation coefficient R^2 of 0.84. These results specify that the MoO_{3-x}-TpTTA COF NC materials as SERS active substrates can fulfil the requirements of quantitative detection. Additionally, the MoO_{3-x}-TpTTA COF NC has demonstrated a prominent SERS response for the detection of a commercial fungicide, with a remarkable detection limit (LOD) of 12.5 ppm. Furthermore, to evaluate the role of nonstoichiometric MoO_{3-x} in MoO_{3-x}-TpTTA COF NC materials for SERS enhancement, the Raman signals of Mz on the only TpTTA COF were recorded, which show a higher LOD of 100 ppm, mostly because of the effective adsorption of the analyte in the COF moiety (Fig. 7d). This effectively confirmed the critical role of MoO_{3-x} in enhancing SERS performance in MoO_{3-x}-TpTTA COF NC materials.

The reproducibility of the SERS signal of Mz was further studied for demonstrating the practical application of the as-synthesized SERS substrate. The Mz solution of 500 ppm concentration was studied to verify the uniformity of the SERS signal obtained from the MoO_{3-x}-TpTTA COF NC substrate. A total of 10 random measuring points were selected from the MoO_{3-x}-TpTTA COF NC SERS substrate, and the results showed that the obtained SERS signals were highly dependable (Fig. 7e). For the characteristic peak at 1140 cm^{-1}, the Raman spectra recorded from 10 points were used to calculate the RSD, as presented in Fig. 7f. The RSD obtained from the calculation was 9.35%, indicating excellent uniformity and measurement reproducibility of the MoO_{3-x}-TpTTA COF NC SERS substrate.[39,40] Thus, in our study, we achieved a detection limit for Mz of 12.5 ppm, which is significantly below the toxicologically relevant levels (~75 ppm) reported by the FAO/WHO.[59]

3.2.4. Long-term storage stability and reusability of the SERS substrate. The SERS detection capabilities of 500 ppm Mancozeb over a four-week period were examined to verify the long-term storage stability of the MoO_{3-x}-TpTTA COF NC SERS substrate, as shown in Fig. S9a (SI). The SERS signal measuring points were randomly selected from the substrate, and the results indicated that the SERS signals were mostly consistent. For a typical characteristic peak at 1140 cm^{-1}, we calculated the relative standard deviation (RSD) from the SERS spectra obtained from the MoO_{3-x}-TpTTA COF NC substrate, as illustrated in Fig. S9b (SI). The RSD was found to be 6.38%, demonstrating the long-term stability, reproducibility, and reliability of the MoO_{3-x}-TpTTA COF NC SERS substrate for pesticide detection.

These results visibly demonstrated that the strong SERS effect was promoted by the oxygen vacancies along with the surface defects, as reported earlier.[38,52,53] This displays that the high sensitivity of detection of analytes, including pesticides, could be achieved *via* oxygen vacancy defects created in the case of MoO_{3-x} in the MoO_{3-x}-TpTTA COF NC *via* a simple and rapid one-step MW-AT synthesis strategy for the first time, which can be further applied for the fabrication of other COF nanocomposite systems. The ultralow detection capability of the MoO_{3-x}-TpTTA COF NC as the SERS substrate with high reproducibility with an LOD as low as 12.5 ppm for Mz, a common commercially used dithiocarbamate insecticide, outperforms other available SERS substrates, even when using noble metals to prepare the COF composite-based SERS substrates. This features as the first report of a nonstoichiometric TMO (MoO_{3-x})-based COF composite used as a SERS substrate (Table S3, SI). This breakthrough paves the way for innovative and scalable solutions to address pressing environmental and public health challenges posed by hazardous agrochemicals.

4. Conclusion

In summary, we have successfully synthesized a TpTTA COF and a nonstoichiometric molybdenum trioxide-TpTTA COF (MoO_{3-x}-TpTTA) nanocomposite using a facile one-step microwave-assisted synthesis method for the first time. This process takes approximately one hour and achieves a high yield at a moderate temperature of 120 °C, in contrast to traditional solution-based COF synthesis methods. The synthesized products were characterized by XRD, IR, UV-vis, XPS, Raman, EPR, NMR, TGA, BET, FESEM, HRTEM, HAADF, and EDS analyses, and the formation mechanism was also proposed. Furthermore, the as-synthesized MoO_{3-x}-COF-based nanocomposite was employed as an affordable and straightforward surface-enhanced Raman scattering (SERS) substrate to detect trace amounts of MB. The nanocomposite exhibited SERS activity with an RSD of 6.10% for SERS reproducibility. The maximum EF reached was up to 7.76×10^4 with a detection limit as low as 1.0×10^{-7} M. The incorporation of MoO_{3-x} into the COF offered several advantages, including SERS enhancement by nonstoichiometric transition metal oxides *via* oxygen vacancy defects, without the need for noble nanocrystals (*e.g.*, Ag, Au, *etc.*), SERS enhancement repeatability, SERS substrate stability, comparative SERS sensitivity, and cost-effectiveness. To the best of our knowledge, this is the first report showcasing efficient, highly stable, and reproducible SERS substrates based on the nonstoichiometric TMO-COF nanocomposite (*i.e.*, MoO_{3-x}-TpTTA) synthesized through a simple inorganic protocol, without any noble metal incorporation, graphene composite, polymer encapsulation, or molecularly imprinted polymer strategies. This is achieved through strategic design and practical synthesis by grafting MoO_{3-x} on the COF to form the MoO_{3-x}-TpTTA COF nanocomposite. Moreover, this study presents the first instance of an ultralow detection capability of the nonstoichiometric TMO-COF nanocomposite-based SERS substrate (MoO_{3-x}-TpTTA), demonstrating high reproducibility, with a limit of detection (LOD) as low as 12.5 ppm. This detection level is significantly below the toxicologically relevant levels reported by the FAO/WHO for Mancozeb, a common, commercially used dithiocarbamate insecticide used on various vegetables, fruits, nuts, and field crops, classified as a category III carcinogen by the International Agency for Research on Cancer. Hence, our methodology opens up numerous possibilities for selecting metal oxide, microwave-based rapid synthesis strategies, and nanocrystal growth environments for the creation of nanocomposite materials. This can lead to the development of stable and efficient nonstoichiometric TMO-based SERS substrates for the quantitative detection of hazardous organic pollutants including pesticide residues in agriculture, food, and environmental contexts. This work also paves the way for designing nonstoichiometric TMO-based SERS substrates for next-generation applications in SERS-based environmental and agricultural/food safety monitoring, representing a strong alternative to conventional noble metal-based SERS techniques in advanced sensing technologies.

Author contributions

Manoj Krishnat Patil: conceptualization, methodology, reproducibility of synthesis, material characterization, fungicide SERS analysis, and writing the initial draft; Premjeet Gangadhar Wagh: MB SERS experiments, data analysis, and the EF, RSD, and correlation coefficient calculations; Shatabdi Porel Mukherjee: conceptualization, methodology, writing, review and editing, funding acquisition, resource gathering, supervision, and validation. The manuscript was written through the contributions of all authors. All authors have approved the final version of the manuscript.

Conflicts of interest

Indian Provisional Patent Application filed; Application number: 202511044493, dated 07-05-2025, entitled "Microwave-assisted synthesis of MoO_{3-x} TP-TTA COF for microlevel detection of mancozeb fungicide using surface-enhanced Raman spectroscopy".

Data availability

The data supporting this article have been included as part of the supplementary information (SI). XPS Survey spectrum, BET isotherm plot, TGA and solid-state NMR of TpTTA COF and MoO_{3-x}-TpTTA COF NC. FESEM, HRTEM, EDS, HAADF-STEM image and elemental mapping of TpTTA COF, images of reaction mixture containing product in glass vial after MW-AT synthesis, MB SERS reproducibility and intensity distribution plot, SERS EF calculations for MoO_{3-x}-TpTTA COF NC, SERS spectra of 500 ppm Mancozeb on MoO_{3-x}-TpTTA COF NC, and

comparison table of MoO_{3-x}-TpTTA COF NC with previously reported COF composites used for pesticide detection. See DOI: https://doi.org/10.1039/d5nr02849c.

Acknowledgements

The authors wish to acknowledge Dr Ashish Lele, Director, CSIR-NCL, for his constant support. The authors would like to acknowledge the NCL grant (project codes: MLP031526 and OLP003326), GAIL India Ltd (project code: GAP324726), the Anusandhan National Research Foundation (ANRF)-core research grant (CRG/2023/006338) with the institute project number GAP340626 (dated 12-03-2024) and the CSIR FIRST research grant (project code: FIR060302, dated 23-07-2024) for financial and infrastructure support. The authors would also like to thank the Central Analytical Facility (CAF, NCL, Pune) for FESEM, HRTEM, and XPS analyses and Dr Rupali Waichal, Ms Rameshwari Nannaware and Ms Jagruti Kurkure for the Raman analysis. The authors wish to acknowledge Mr Aniruddha Kurlekar for the BET analysis, Prof. Sujit K. Ghosh, Mr Anirban Roy, IISER Pune and Prof. Sanjib Kar, Ms Rwiddhi Chakraborty, NISER,Bhubaneswar for the EPR spectroscopy analysis and Ms Nita Patil for solid state NMR analysis. The authors also thank Mr Yogesh Kumar and Dr Sreekumar Kurungot for the TGA analysis. MKP thanks SARTHI, Govt. of Maharashtra, for a CSM National Research Fellowship, and PGW thanks UGC for a Junior Research Fellowship.

References

1 K. Geng, T. He, R. Liu, S. Dalapati, K. T. Tan, Z. Li, S. Tao, Y. Gong, Q. Jiang and D. Jiang, *Chem. Rev.*, 2020, **120**, 8814–8933.
2 Y. Zhu, L. Chen, J. Pan, S. Jiang, J. Wang, G. Zhang and K. Zhang, *Prog. Mater. Sci.*, 2025, **148**, 101373.
3 S. J. Lyle, T. M. Osborn Popp, P. J. Waller, X. Pei, J. A. Reimer and O. M. Yaghi, *J. Am. Chem. Soc.*, 2019, **141**, 11253–11258.
4 J. Liu, N. Wang and L. Ma, *Chem. – Asian J.*, 2020, **15**, 338–351.
5 X. Liu, D. Huang, C. Lai, G. Zeng, L. Qin, H. Wang, H. Yi, B. Li, S. Liu, M. Zhang, R. Deng, Y. Fu, L. Li, W. Xue and S. Chen, *Chem. Soc. Rev.*, 2019, **48**, 5266–5302.
6 Z. Meng and K. A. Mirica, *Chem. Soc. Rev.*, 2021, **50**, 13498–13558.
7 N. Keller and T. Bein, *Chem. Soc. Rev.*, 2021, **50**, 1813–1845.
8 M. Lv, X. Wu, W. Wang, D. Han, S. Chen, Y. Hu, Q. Zhang, Q. Wang and R. Wei, *ACS Sens.*, 2025, **10**, 1778–1787.
9 X. Jiang, J. Fu, D. Li, W. Xue and Y. Zhang, *Anal. Lett.*, 2024, **57**, 2455–2468.
10 O. Guselnikova, H. Lim, H. J. Kim, S. H. Kim, A. Gorbunova, M. Eguchi, P. Postnikov, T. Nakanishi, T. Asahi, J. Na and Y. Yamauchi, *Small*, 2022, **18**, 2107182.
11 M. Liu, L. Guo, S. Jin and B. Tan, *J. Mater. Chem. A*, 2019, **7**, 5153–5172.
12 X. Chen, Y. Li, L. Jia, X. Yu, Q. Wang, Y. Zhang, Z. Zhang, E. Liang, B. Han and J. Li, *J. Solid State Chem.*, 2023, **328**, 124352.
13 M. Hussain, A. Saddique, K. C. Devarayapalli, B. Kim, I. W. Cheong and D. S. Lee, *Appl. Catal., B*, 2024, **344**, 123672.
14 G. Dai, Q. Zhang, S. Xiong, L. Deng, Z. Gao, A. Chen, X. Li, C. Pan, J. Tang and G. Yu, *J. Membr. Sci.*, 2023, **676**, 121561.
15 L. Sun, W. Wang, T. Kong, H. Jiang, H. Tang and Q. Liu, *J. Mater. Chem. A*, 2022, **10**, 22531–22539.
16 Y. Wang, A. Pan, Y. Ma and H. Du, *Int. J. Hydrogen Energy*, 2024, **72**, 1298–1307.
17 R. Gao, J. Bai, R. Shen, L. Hao, C. Huang, L. Wang, G. Liang, P. Zhang and X. Li, *J. Mater. Sci. Technol.*, 2023, **137**, 223–231.
18 G. Zhao, Y. Sun, Y. Yang, C. Zhang, Q. An and H. Guo, *EcoMat*, 2022, **4**, 1–12.
19 X. Wang, L. Sun, W. Zhou, L. Yang, G. Ren, H. Wu and W. Q. Deng, *Cell Reports Phys. Sci.*, 2022, **3**, 100804.
20 N. Yuan, C. Zhang, X. Zhang and R. Zhang, *J. Cleaner Prod.*, 2024, **434**, 140259.
21 F. Omori, I. Tateishi, H. Katsumata, M. Furukawa and S. Kaneco, *Colloids Surf., A*, 2025, **705**, 135655.
22 T. Zhang, Y. Xia, Y. D. Xie, H. J. Du, Z. Q. Shi, H. L. Hu, H. Zhang, Z. C. Guo and G. Li, *J. Colloid Interface Sci.*, 2024, **665**, 554–563.
23 Z. C. Guo, M. L. You, Z. J. Wang, Z. F. Li and G. Li, *ACS Appl. Mater. Interfaces*, 2022, **14**, 15687–15696.
24 J. Wang, Y. Yu, J. Cui, X. Li, Y. Zhang, C. Wang, X. Yu and J. Ye, *Appl. Catal., B*, 2022, **301**, 120814.
25 H. Dai, H. Li and Q. Yang, *Microporous Mesoporous Mater.*, 2022, **342**, 112121.
26 S. Kunjattu H, N. M. Thorat, S. Gawas and U. K. Kharul, *ACS Appl. Mater. Interfaces*, 2024, **16**, 19463–19471.
27 Y. Zhang, H. Ye, D. Chen, N. Li, Q. Xu, H. Li, J. He and J. Lu, *J. Membr. Sci.*, 2021, **628**, 119216.
28 K. Dey, S. Kunjattu H, A. M. Chahande and R. Banerjee, *Angew. Chem.*, 2020, **132**, 1177–1181.
29 B. Lyu, M. Wang, J. Jiang and Z. Jiang, *J. Membr. Sci.*, 2022, **662**, 120976.
30 Y. Qiu, C. Jiang, X. Xin, Y. Y. Li, H. Wang, J. Xu, H. Lin, L. Wang and V. Turkevich, *ACS Appl. Nano Mater.*, 2024, **7**, 11234–11247.
31 K. Chen, A. Cai and T. T. Li, *ChemSusChem*, 2023, **16**, 1–23.
32 J. Zhang, M. Zhou, L. Yang, B. Huang, K. Lu, H. Wen and J. Ren, *Sens. Actuators, B*, 2025, **422**, 136609.
33 Y. Xie, Q. Li, J. Chen, W. Yue, Z. Xia, M. Zeng, Y. He, Y. Zhao and X. Luo, *Sens. Actuators, B*, 2023, **394**, 134470.
34 Y. M. Shirke and S. Porel Mukherjee, *CrystEngComm*, 2017, **19**, 2096–2105.
35 S. H. Gaikwad and S. Porel Mukherjee, *Environ. Sci. Nano*, 2022, **9**, 4508–4523.
36 V. Jeyavani and S. Porel Mukherjee, *Inorg. Chem.*, 2022, **61**, 18119–18134.
37 M. K. Patil, S. H. Gaikwad, A. A. Balachandran Kirali, B. Marimuthu and S. Porel Mukherjee, *ACS Appl. Nano Mater.*, 2023, **6**, 22635–22642.

38 M. K. Patil, S. H. Gaikwad and S. Porel Mukherjee, *J. Phys. Chem. C*, 2020, **124**, 21082–21093.
39 S. H. Gaikwad and S. Porel Mukherjee, *ACS Appl. Nano Mater.*, 2021, **4**, 11611–11624.
40 R. Wu, X. Song and G. Tian, *Environ. Sci. Pollut. Res.*, 2024, **31**, 44759–44769.
41 J. Runkle, J. Flocks, J. Economos and A. L. Dunlop, *Environ. Int.*, 2017, **99**, 29–42.
42 Y. Li, W. Chen, G. Xing, D. Jiang and L. Chen, *Chem. Soc. Rev.*, 2020, **49**, 2852–2868.
43 B. Díaz de Greñu, J. Torres, J. García-González, S. Muñoz-Pina, R. de los Reyes, A. M. Costero, P. Amorós and J. V. Ros-Lis, *ChemSusChem*, 2021, **14**, 208–233.
44 H. Wei, S. Chai, N. Hu, Z. Yang, L. Wei and L. Wang, *Chem. Commun.*, 2015, **51**, 12178–12181.
45 R. Gomes, P. Bhanja and A. Bhaumik, *Chem. Commun.*, 2015, **51**, 10050–10053.
46 J. Yu, Z. Zheng, A. Wang and M. Humayun, *Nanomaterials*, 2024, **14**, 1189.
47 R. K. Nitharwal, A. Sahoo, V. Kumar, M. S. R. Rao, T. Dixit and S. Krishnan, *ACS Mater. Lett.*, 2025, **7**, 1195–1202.
48 P. Kour and S. Porel Mukherjee, *J. Mater. Chem. A*, 2021, **9**, 6819–6826.
49 N. Sakhuja, R. Jha and N. Bhat, *Mater. Sci. Eng., B*, 2021, **271**, 115249.
50 W. Sun, X. Tang, Q. Yang, Y. Xu, F. Wu, S. Guo, Y. Zhang, M. Wu and Y. Wang, *Adv. Mater.*, 2019, **31**, 1903176.
51 Y. Li, J. Cheng, Y. Liu, P. Liu, W. Cao, T. He, R. Chen and Z. Tang, *J. Phys. Chem. C*, 2017, **121**, 5208–5214.
52 X. Hou, X. Fan, P. Wei and T. Qiu, *J. Mater. Chem. C*, 2019, **7**, 11134–11141.
53 X. Du, D. Liu, K. An, S. Jiang, Z. Wei, S. Wang, W. F. Ip and H. Pan, *Appl. Mater. Today*, 2022, **29**, 101563.
54 F. Kong, S. Zhang and S. Ding, *J. Appl. Polym. Sci.*, 2024, **141**, 1–7.
55 Y. Ying, M. Fang, C. Wang, Z. Yan, H. Xie, W. Wu, Z. Tang and Y. Liu, *Small*, 2025, 2501846.
56 A. Walia, P. Mehta, S. Guleria, A. Chauhan and C. K. Shirkot, *Sci. World J.*, 2014, **2014**, 702909.
57 C. M. Tsen, C. W. Yu, S. Y. Chen, C. L. Lin and C. Y. Chuang, *Appl. Surf. Sci.*, 2021, **558**, 149740.
58 P. A. Atanasov, N. N. Nedyalkov, N. Fukata, W. Jevasuwan, T. Subramani, D. Hirsch and B. Rauschenbach, *AIP Conf. Proc.*, 2019, **2075**, 030001.
59 G. Vettorazzi, W. F. Almeida, G. J. Burin, R. B. Jaeger, F. R. Puga, A. F. Rahde, F. G. Reyes and S. Schvartsman, *Teratog., Carcinog., Mutagen.*, 1995, **15**, 313–337.